inventions

MDPI

Communication

Performance Evaluation of Photonics-Based Coherent MIMO Radar Systems for Maritime Surveillance

Malik Muhammad Haris Amir [1,*], Salvatore Maresca [2], Gaurav Pandey [1], Antonio Malacarne [3], Antonella Bogoni [1,3] and Mirco Scaffardi [3]

[1] Institute of Technologies of Communication, Information, and Perception (TeCIP), Scuola Superiore Sant'Anna, 56124 Pisa, Italy; gaurav.pandey@santannapisa.it (G.P.); antonella.bogoni@santannapisa.it (A.B.)
[2] Institute of Electronics, Information Engineering and Telecommunications (IEIIT), Consiglio Nazionale delle Ricerche (CNR), 56124 Pisa, Italy; salvatore.maresca@cnr.it
[3] National Inter-University Consortium for Telecommunications (CNIT), 56124 Pisa, Italy; antonio.malacarne@cnit.it (A.M.); mirco.scaffardi@cnit.it (M.S.)
* Correspondence: malikmuhammadharis.amir@santannapisa.it

Abstract: Multiple-input multiple-output (MIMO) radars offer significant advantages over conventional standalone radars in terms of target detection and localization capabilities. However, to fully exploit their potential, such systems require excellent time and phase synchronization among the central unit and the radar heads. Only recently, thanks to microwave photonics (MWP) techniques, it has been possible to develop the first coherent MIMO radar demonstrators. In this paper, a simulation tool in MATLAB programming language is proposed to model coherent MIMO radars based on MWP techniques in maritime surveillance applications. Moreover, a novel approach for estimating the radar cross section of extended maritime targets is presented. The system performance in co-located and distributed MIMO configuration, as well as in single- and multi-band operations, is evaluated by means of relevant key performance indicators (KPIs). Simulations are carried out in two close-to-reality scenarios. In the first, a co-located MIMO radar is mounted on top of a patrolling vessel. In the second, a distributed MIMO radar is deployed inside a port. The proposed KPIs are analyzed in terms of both geometric and frequency diversities of the system, laying the foundations for general system optimization criteria valid in any given surveillance application.

Keywords: MIMO radars; microwave photonics; system simulator; ambiguity function; frequency diversity; geometric diversity; key performance indicators; maritime surveillance; RCS model

Citation: Amir, M.M.H.; Maresca, S.; Pandey, G.; Malacarne, A.; Bogoni, A.; Scaffardi, M. Performance Evaluation of Photonics-Based Coherent MIMO Radar Systems for Maritime Surveillance. *Inventions* **2023**, *8*, 99. https://doi.org/10.3390/inventions8040099

Academic Editors: Timofey Shevgunov and Antonio Napolitano

Received: 3 July 2023
Revised: 31 July 2023
Accepted: 4 August 2023
Published: 7 August 2023

1. Introduction

Since its inception, radar technology has undergone continuous research and advancements both in system architecture and processing domain to satisfy the rising performance demands [1]. In recent decades, multiple-input multiple-output (MIMO) radar technology employing multiple transmitters (TXs) and multiple receivers (RXs) has emerged as a promising technology to overcome the constraints of conventional standalone radar systems [2].

Based on antenna separation compared to the target range, MIMO radars can be divided into two categories: (i) co-located systems with closely spaced antennas, and (ii) distributed systems with widely separated antennas. The former offers superior flexibility and improved parameter estimation in transmit beam design when compared to traditional phased array radars [3], whereas the latter offers excellent geometric diversity for mitigating the issue of radar cross section (RCS) fluctuations [4,5].

MIMO radar benefits come at the expense of added complexity, and the system requires excellent time and phase synchronization among the central unit (CU) and the radar heads (RHs). It is challenging to accomplish this using oscillator solely based on radio frequency (RF) technology. In response, hybrid microwave photonics (MWP) have

emerged as a potential enabling technology to make these ideas a reality. Owing to this, a new generation of photonics-based radars have been developed in the past decade [6–8]. Photonics-based MIMO radars can offer excellent geometric diversity (GD), and can also be associated with employing frequency diversity (FD), which is achieved when RHs operate on multiple frequency carriers, thus improving the system resolution.

Given the variety of MIMO radar configurations, including co-located and distributed systems, as well as single- and multi-band systems, assessing the performance of MIMO radars is not a straightforward operation. Therefore, to accurately evaluate the performance of MIMO radars, development of a simulation tool able to simulate different close-to-reality scenarios based on user requirements and definition of key performance indicators (KPIs) is of primary importance. In [9], relevant KPIs were proposed for the characterization of the MIMO Ambiguity Function (MIMO-AF). Thus, KPIs represent the general criteria for system optimization valid in any given surveillance application.

Recently, a work has been presented that discusses the criteria for defining the optimal coherent multistatic radar network [10]. In this work, a simulation tool, developed in MATLAB programming language, is proposed to model coherent MIMO radar systems operated using MWP techniques. Compared to the other simulators already existing in literature such as [11,12], which are developed for automotive applications using co-located MIMO radar networks, the simulator presented in this work is quite flexible, being able to simulate different waveforms and simulation scenarios involving both co-located and distributed MIMO radar networks using photonics depending on user preferences. Moreover, a novel and computationally efficient approach for estimating the RCS of extended maritime targets is presented and incorporated in the simulator. Simulations are carried out in two close-to-reality use-cases: (i) a shipborne scenario where a co-located MIMO radar network is mounted on top of 100 m long surveillance vessel, and (ii) a ground-based scenario, where a distributed MIMO radar network is deployed in a port area of Livorno, Italy. For these use-cases, both single- and multi-band operation are considered. Finally, system performance is evaluated running the simulation tool in two use-cases.

The document is structured as follows. Section 2 describes the simulation tool developed in MATLAB programming language. First, coherent MIMO processing is presented and then a novel method for the approximation of target RCS is proposed. Moreover, in this section, the functionalities and design parameters that are used in the simulator are also highlighted. Sections 3 and 4 focus on identifying relevant KPIs and simulation scenarios, respectively. Section 5 deals with the result and analysis of identified KPIs for two use-case scenarios in terms of geometric and frequency diversities. Then, the conclusions are provided in Section 6, together with the future challenges.

2. Coherent Multi-Band MIMO Radar

Consider a system consisting of M TXs and N RXs denoted as TX_m and RX_n respectively, where $m = 1, \ldots, M$ and $n = 1, \ldots, N$.

2.1. MIMO Signal Model and Processing

Let us assume that the antennas illuminate K point scatterers P_k, where $k = 1, \ldots, K$. These scatterers can generally belong to one or more targets in a surveyed space. Moreover, let us assume that all M TXs operate at L carriers. Thus, the signal transmitted by TX_m at lth frequency is denoted by $S_{m,l}(t)$, where $l = 1, \ldots, L$. The signal received by RX_n can be written as [4]:

$$r_{m,n,l}(t) = \sum_{k=1}^{K} a_{m,n,l}^{(k)} s_{m,l}\left(t - \tau_{m,n}^{(k)}\right) e^{j\varphi_{m,n,l}(t)} + w_{n,l}(t) \quad (1)$$

where $a_{m,n,l}^{(k)}$ and $\tau_{m,n}^{(k)}$ denote the complex amplitude and the delay from scatterer P_k observed by TX_m and RX_n at lth carrier frequency, and $\varphi_{m,n,l}(t)$ accounts for the overall phase shift introduced by the architecture.

For easiness, in Equation (1), the term $w_{n,l}(t)$ is modelled as additive white Gaussian noise (AWGN) with unitary power, while $a_{m,n,l}^{(k)}$ and $\tau_{m,n}^{(k)}$ depend on the bistatic geometry among TX_m, RX_n and P_k:

$$a_{m,n,l}^{(k)} = \sqrt{\frac{P_{TX}^{(m,l)} G_{TX}^{(m,l)} A_{n,l} \sigma_{m,n,l}^{(k)}}{(4\pi)^3 k_B B_{n,l} T_n L_n \boldsymbol{d}^2(TX_m, P_k) \boldsymbol{d}^2(P_k, RX_n)}} \tag{2}$$

$$\tau_{m,n}^{(k)} = \frac{1}{c}[\boldsymbol{d}(TX_m, P_k) + \boldsymbol{d}(P_k, RX_n)], \tag{3}$$

Here, $P_{TX}^{(m,l)}$ and $G_{TX}^{(m,l)}$ are the transmit power and antenna gain at TX_m of lth waveform, respectively, $A_{n,l}$ is the effective area of the RX_n at lth carrier $f_{RF}^{(l)}$, $\sigma_{m,n,l}^{(k)}$ is the bistatic RCS of scatterer P_k observed by TX_m and RX_n, k_B is the Boltzmann's constant, c is the speed of light, $B_{n,l}$ is the noise bandwidth, and T_n and L_n are the noise temperature and the loss factor at RX_n, respectively. Finally, $\boldsymbol{d}(TX_m, P_k)$ and $\boldsymbol{d}(P_k, RX_n)$ are the Euclidean distances between TX_m and P_k, and P_k and RX_n, respectively.

The proposed MIMO radar leverages on a centralized processing architecture. The target position can be determined from the maximum of the log-likelihood function of the target at location $\vec{X}$ evaluated from all $M \times N \times L$ received signals. The coherent MIMO-AF can be calculated as [4]:

$$A_C\left(\vec{X}\right) \triangleq \frac{1}{(MNL)^2} \left| \sum_{m=1}^{M} \sum_{n=1}^{N} \sum_{l=1}^{L} E_l(\tau_{m,n}) \cdot \Psi_{m,n,l}(t, \tau_{m,n}) \right|^2 \tag{4}$$

where $\Psi_{m,n,l}(t, \tau_{m,n})$ represents the cross-correlation between $r_{m,n,l}(t)$ and $s_{m,l}(t)$, whereas $E_l(\tau_{m,n}) \triangleq e^{-j2\pi f_{RF}^{(l)} \tau_{m,n}}$ are exponential terms depending on the lth RF carrier and $\tau_{m,n}^{(k)}$ underlying bistatic geometry among TX_m, RX_n and P_k.

2.2. System Simulator

The simulation tool implements several functionalities and options that are multi-band operation, radar system and antenna parameters (e.g., position, transmitted power, antenna gain, antenna aperture), waveform parameters (e.g., type, carrier frequency, pulse duration, signal bandwidth, pulse repetition interval (PRI)), transmission diversity (e.g., time division multiplexing (TDM), frequency division multiplexing (FDM)), system non-idealities (e.g., additive noise, not exact antenna position, mismatch among channel amplitudes/phases, phase noise), with a possibility to synchronize/calibrate the radar channels, using Monte Carlo simulations.

All the functionalities of the tool are developed around the definition of some ad hoc option/keywords for setting up the simulation parameters and evaluating the outputs required by the user. The tool allows the user to choose among different types of baselines (e.g., linear, circular, coastal-based and shipborne). Selections have been included for calculating different types of outputs (e.g., non-coherent MIMO, coherent MIMO), different adaptive beamforming algorithms (least squares (LS) [13], Capon [14] and robust Capon beamformer (RCB) [15] ...), options for selecting the processing to be employed (e.g., single or multi-pulse, single or multi-band) and for displaying the results. Some options/keywords are defined for assigning both sensor and waveform parameters. Among the available waveforms, the user can choose among un-modulated pulses, linear frequency modulated (LFM) pulses, bi-phase codes (e.g., Barker and pseudo-random binary sequences (PRBS)), poly-phase codes (e.g., Frank, P3 and P4 codes) and stepped frequency (SF) waveforms with fixed frequency increments and Costas codes, with pseudo-random frequency jumps instead.

The simulation tool allows the user to also consider general system non-idealities. Among these, the user can select to consider AWGN, signal-to-noise ratio (SNR) decrease

according to the radar equation, random time offsets of radar channels, phase noise induced by optical fiber distribution vibrations, unknown antenna position mismatches and amplitude mismatch among the radar channels. The possibility to run algorithms for correcting such non-idealities is also implemented in the simulator.

The main operational steps of the simulation tool are presented in Figure 1. In the first block, the simulation parameters (e.g., TX and RX locations, waveform and antenna parameters, system non-idealities, target kinematics, target size) are assigned by the user. In the second block, based on the TX, RX position provided in block 1, the relative target-sensor geometry is retrieved for all the targets and TX/RX sensors and condensed in the delays $\tau_{m,n}^{(k)}$, which are calculated according to Equation (3).

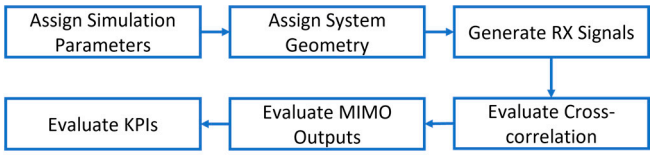

Figure 1. Operational Steps of MIMO Radar System Simulator in MATLAB.

In the third block, the received signals $r_{m,n,l}(t)$ are evaluated using Equation (1), which considers the waveform parameters (provided by user in block 1), the relative target-sensor geometry, as well as the RCS value, which is obtained according to the methodology presented in Section 2.3. Cross-correlations $\Psi_{m,n,l}(t, \tau_{m,n})$ are evaluated in the fourth block for $m = 1, \ldots, M$, $n = 1, \ldots, N$, and $l = 1, \ldots, L$. Before this step, the received signals are first down-converted to the selected intermediate frequency (IF), or directly at baseband (BB). Then, they are down-sampled to lighten the computational burden. For each of the available radar channels, the down-converted/down-sampled received signals are cross-correlated with the reference signals. This is necessary for the successive evaluation of the non-coherent/coherent MIMO outputs.

In the fifth block, the coherent MIMO-AF is then evaluated according to Equation (4). Finally, the KPIs are evaluated from the coherent MIMO-AF in the sixth block of the simulator. The KPIs are evaluated for all the available/selected MIMO processing outputs. The tool estimates the following performance metrics: range (dR), cross-range (dXR) and area (dA) resolution at -3 dB of the main lobe, peak-to-maximum sidelobe ratio (PMSR) and peak-to-average sidelobe ratio (PASR). In this paper, we analyze the performance of MIMO radar networks using the aforementioned KPIs.

2.3. RCS Modeling

The RCS refers to the electromagnetic area of the target, proportional to the amount of power scattered from the target of interest towards the direction of the receiver, when target itself is illuminated by the transmitted RF signal [16]. In case of moving target, where the target orientation with respect to RHs is continuously varying, a special importance must be paid for evaluating the bistatic RCS ($\sigma_{m,n,l}^{(k)}$).

Target RCS estimation models can be divided into two categories, i.e., exact, and approximate methods [17]. To save the computational burden, approximate solutions are most commonly used instead of exact solutions [18]. Previously, a well-known approximate method based on physical optics (PO) technique, i.e., POfacets software developed for MATLAB [19] has been used to calculate RCS. However, given a close-to-reality scenario where the target orientation is continuously changing, estimating RCS using POfacets can be computationally expensive. Therefore, another level of approximation based on empirical formula is applied to obtain the bistatic RCS of a naval target of length L.

First, a monostatic RCS is derived using empirical formula [20]:

$$\sigma_M^{(L)} = 52 f^{\frac{1}{2}} D^{\frac{3}{2}} \tag{5}$$

where f is the operating frequency and D is the displacement of the vessel. Given the length of the vessel L, it is possible to obtain the vessel displacement D by interpolating the values as described in [21]. Then, by applying Equation (5), monostatic RCS is calculated at selected carrier. Note that the RCS obtained from Equation (5) is only dependent on target's displacement and not on target orientation with respect to the RHs. Hence, to introduce as an additional design parameter the illumination angle of target, POfacets is used. POfacets approximate the target surface by several triangular surfaces, called "facets", on which the induced surface currents are calculated. Instead, the surface current of facets that are not illuminated is set to zero. The final RCS is proportional to the coherent sum of all these currents. The detailed function of POfacets can be found in [22]. Given the direction of arrival θ, the monostatic RCS can be calculated as follows:

$$\sigma_M^{(L)}(\theta) = \frac{\langle \sigma_M^{(L)} \rangle \cdot}{\langle \sigma_M^{(Lo)} \rangle} \sigma_M^{(L_0)}(\theta) \tag{6}$$

where, $\sigma_M^{(L_0)}(\theta)$ is the monostatic RCS depending on the angle of arrival θ for a single 3D target model of a yacht of length $L_0 = 40$ m. The term $\langle \sigma_M^{(L)} \rangle / \langle \sigma_M^{(Lo)} \rangle$ provides the approximate proportionality coefficient between the monostatic RCS of a target of length L and the monostatic RCS of the model target of length L_0. Equation (5) provides the complete information of monostatic RCS depending on its direction of arrival with respect to the receiving RH. Note that for the sake of POfacets simulations, the bow and stern of the target is considered at $\theta = 0^0$ and 180^0, respectively.

To estimate the bistatic RCS of target, it is necessary to introduce bistatic angle β (i.e., the angle subtended by the TX and the RX at the target position). In fact, the main source of variation in the bistatic radar case is due to the variations in the respective angles of TX and RX to the target [23]. The ratios between the median bistatic RCS and the median monostatic RCS values as a function of β were evaluated from in-field acquisitions, see Figure 2 (blue triangles). These ratios tend to decrease with increasing bistatic angle from 0° (i.e., monostatic case) to 90°. By simplification assumption, values from 90° to 180° (i.e., forward scattering case) are obtained by mirroring values from 90° to 0° around 90° [24].

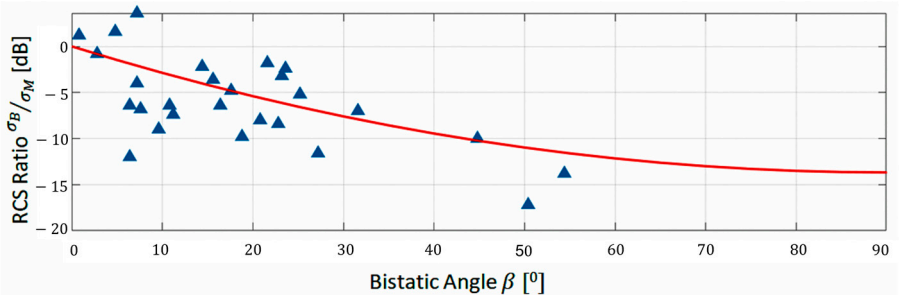

Figure 2. Ratio between bistatic (σ_B) and monostatic (σ_M) RCS as a function of the bistatic angle. Image adapted from [23], in-field acquisitions represented with blue triangles while red curve represents the fitted data.

By fitting the ratios in Figure 2 (red curve), bistatic RCS of a vessel of length L at the varying of θ and β can be calculated as follows:

$$\sigma_B^{(L)}(\theta, \beta) = \sigma_M^{(L)}(\theta) \cdot \frac{\sigma_B}{\sigma_M}(\beta) \tag{7}$$

Note that, for $\beta = 0°$, Equation (7) gives exactly the monostatic RCS as the output. The evaluation of the bistatic angle β is performed according to the relative target-sensor geometry. The pseudo-code of the proposed methodology is presented in Algorithm 1.

Algorithm 1. Pseudo-code of proposed methodology for RCS estimation

Set Simulation Parameters
  DO: Get displacement D from vessel of length L;
  FOR l = 1: L (Number of Frequency Carriers)
    DO: Calculate $< \sigma_M^{L_0} >$ for ship model of length $L_0 = 40$ m, using (5)
    DO: Calculate $< \sigma_M^{(L)} >$ for ship model of length L and displacement D, using (5)
  END
Calculate Monostatic/Bistatic RCS
  FOR m = 1: M (Number of Transmitters)
    DO: Evaluate illumination angle θ;
    FOR n = 1: N (Number of Receivers)
      DO: Evaluate bistatic angle β given transmitter-target-receiver geometry;
      DO: calculate ratio $\frac{\sigma_B}{\sigma_M}(\beta)$ between bistatic and monostatic RCS;
      FOR l = 1: L (Number of Frequency Carriers)
        DO: Calculate $< \sigma_M^{L_0}(\theta) >$ using POFACETS tool;
        DO: Calculate $< \sigma_M^{(L)}(\theta) >$ using (6);
        DO: Calculate $< \sigma_B^{(L)}(\theta, \beta) >$ using (7);
      END
    END
  END

In Figure 3, the RCS of a sample maritime target is calculated as a function of bistatic angle (β), considering the proposed approach (yellow curve), POfacets (blue circles) and moving average of RCS calculated using POfacets (red curve). It is worth noticing that in our method, we have devised a technique that involves mirroring data from the 0–90 degrees interval (depicted in Figure 2) to approximate the data in 90 to 180 degrees interval. This approach represents a highly simplified model intended to expedite the evaluation of RCS, since during the simulation, it is quite impractical to calculate the exact bistatic angle at all times due to inherent computational constraints. As depicted in Figure 3, the RCS obtained from our approach is less accurate but follows the same trend to that of the POfacets. However, given the advantages it offers in terms of computation burden, it is a trade-off worth considering. Especially, given that RCS calculation is only a small part of the simulation tool under discussion in this paper.

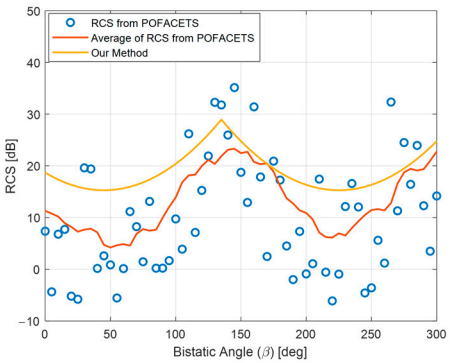

Figure 3. Comparison of bistatic RCS (σ_B) obtained using proposed method (yellow curve), POfacets (blue circles) and moving average of RCS from POfacets (red curve).

2.4. Assessment of Simulation Tool

To assess the effectiveness of the proposed simulation tool, the dual-band coherent MIMO AF of a down-scaled experimental co-located MIMO radar network operating in an indoor environment using two TXs and four RXs in a 3 m long baseline [25] is compared to the dual-band coherent MIMO AF calculated by using simulation tool in the same configurations. The two outputs are plotted in Figure 4. The operating frequencies are set at 8 and 9 GHz, with the bandwidth of 0.4 GHz. As can be seen from the Figure 4a,b, the

two MIMO AFs are quite similar, the main difference between the two is the presence of spurious sidelobes in experimental results, which arise due to the non-idealities of channel amplitudes, phase noise and unpredictable multipath scattering features of the background in the indoor experiment.

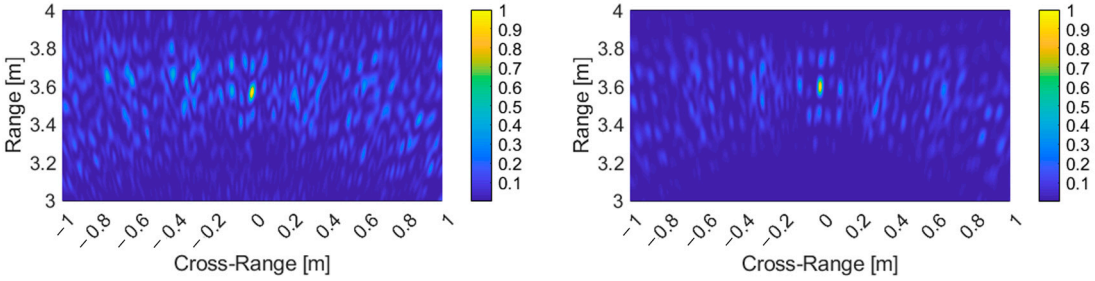

(**a**) (**b**)

Figure 4. Dual-band 2 × 4 MIMO Ambiguity Function for: (**a**) Coherent MIMO processing for dual-band experimental data; (**b**) Coherent MIMO processing for dual-band simulated data.

An embryonal version of the simulation tool was used in [25]. Here, simulations were used to assess the quality of the photonics-based MIMO radar and to foretell the MIMO-AF behavior under more complex system configurations. Moving from these preliminary results, the areas of improvement of the simulator were identified.

Since the experiment, the simulator has been significantly improved. It is now able to simulate extended close-to-reality and complex scenarios. This means that the simulator can now be used to test the performance of a new system in a more realistic environment.

3. Key Performance Indicators

The MIMO radar effectiveness can be evaluated in terms of its capability of detecting, localizing, and resolving a target, as well as suppressing the harmful sidelobes that may appear in the MIMO-AF. The shape of the MIMO-AF is tightly related to both geometric and frequency diversities.

The former (i.e., GD) impacts the capability of the MIMO radar to detect and localize a target observed from different viewpoints. Instead, the latter (i.e., FD) may affect the target resolution capability when the system works at different frequencies. In multi-band distributed MIMO radars, the effect of FD may add constructively to the effect of GD. Thus, following KPIs are considered, according to definitions in [9].

3.1. Peak-to-Sidelobe Ratios of MIMO Ambiguity Functions

The MIMO-AF is the sum of AFs from all the radar channels. The absolute maximum of the MIMO-AF corresponds to the main lobe. Instead, the local maxima are the sidelobes, due to antenna sparseness. Evaluating the sidelobe level is important, since sidelobes may degrade the target detection capability leading to false alarms. Therefore, specific KPIs have been identified to evaluate the robustness of MIMO radars against sidelobes: the peak-to-maximum (PMSR) and the peak-to-average (PASR) sidelobe ratios [9].

$$PMSR \triangleq \frac{max_{\bar{k}\in K}\{AF_c(\bar{k})\}}{max_{k\in K/\bar{k}}\{AF_c(k)\}} \tag{8}$$

$$PASR \triangleq \frac{max_{\bar{k}\in K}\{AF_c(\bar{k})\}}{mean_{k\in K/\bar{k}}\{AF_c(k)\}} \tag{9}$$

where $AF_c(k)$ is coherent MIMO AF value corresponding to kth local maximum, $AF_c(\bar{k})$ corresponds to absolute maximum AF, i.e., main lobe, and K is the total number of local maximums.

3.2. Range, Cross-Range and Area Resolution

Range resolution (dR) refers to the ability of radar system to distinguish between two closely spaced targets along the line-of-sight direction. In MIMO radar context, the range resolution can be improved employing multi-band operation, where transmitters operating on multiple frequency carriers are employed. Therefore, to evaluate the improvement in dR of MIMO radars by employing FD, a KPI has been identified, i.e., resolution gain vs. FD [9].

Cross-range resolution (dXR) refers to the ability of radar system to distinguish between two closely spaced in the plane perpendicular to the line-of-sight. Improvement in cross-range resolution is strictly related to the number of virtual channels in MIMO radar systems. In [23], the improvement in cross-range resolution is demonstrated when the total number of virtual channels is increased. In this paper, stepping from the results in [9], we will evaluate the effect of GDP employed in the two use-cases explained in Section 4 on the dXR.

Finally, area resolution (dA) refers to the ability of MIMO radar to distinguish between two closely spaced targets in both line-of-sight plane and plane perpendicular to line-of-sight.

4. Simulation Scenarios

Based on the analysis conducted in [9], the performance of MIMO radar system can be improved by increasing the number of virtual channels. Increasing the number of virtual channels can improve range and cross-range resolution and decrease the level of sidelobes significantly. However, increasing the number of virtual channels would also add to the complexity and cost of the system. Therefore, a trade-off is required between complexity and performance. Owing to this, the MIMO radar with two TXs and four RXs operating at three frequency carriers was simulated in shipborne scenario and MIMO radar with three TXs and three RXs operating at three frequency carriers was simulated for shore-based scenario, keeping the total number of virtual channels at 24 and 27, respectively.

4.1. Shipborne MIMO Radar Network

In the first scenario, the MIMO radar is installed on top of a 100 m long surveillance vessel. The radar network consists of two TXs and four RXs located along a linear baseline as represented in Figure 5a. The center of the MIMO baseline on the surveillance vessel is at coordinates (0, −100) m, with the antennas deployed along the abscissas. The TX1 and TX2 are at coordinates (−50, +25) m, respectively, whereas RX1, RX2, RX3 and RX4 are at coordinates (−25, −10, +10, +50) m, respectively. A target approaches the surveillance vessel from two trajectories represented in green (Trajectory 1) and magenta points (Trajectory 2) in Figure 5a.

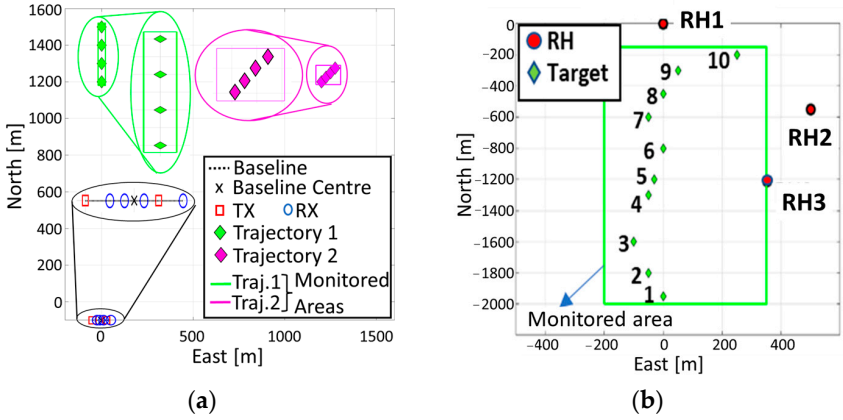

Figure 5. Simulation Scenario for: (**a**) Antenna baseline on the surveillance ship (Tx: blue squares, Rx: red circles), target trajectory 1 (green diamonds) and target trajectory 2 (magenta diamonds); (**b**) Target trajectory (green diamonds) and RHs position (blue triangles) of the MIMO radar in East-North-Up coordinates.

4.2. Ground-Based MIMO Radar Network

In the second scenario, the MIMO radar is ground-based and consists of three RHs, all acting both as TX and RX, operating both in monostatic and bistatic configurations. The system geometry is inspired by a MIMO radar demonstrator deployed at port of Livorno, Italy. The geodetic coordinates of the three RHs are as follows:

- RH1: [10°17′29.6″ E, 43°33′30.1″ N]
- RH2: [10°17′50.1″ E, 43°33′11.2″ N]
- RH3: [10°17′45.3″ E, 43°32′57.3″ N]

The target is a boat entering the port from south according to the trajectory shown in Figure 5b.

In both simulation scenarios, the system employs the parameters summarized in Table 1. These parameters have been chosen such that they are in quite close agreement to the values identified and used in the real operative scenarios described in [26]. The only two relevant exceptions are the employed carrier frequencies (i.e., 8, 9 and 10 GHz) and signal bandwidth (i.e., 600 MHz). The reason is that, as described in [9,25], the sidelobe suppression capability along range of multi-band MIMO radars strongly depends on the separation among carriers. The sparser are the carriers with respect to the signal bandwidths, the higher the sidelobes along range. Thus, carrier frequencies and bandwidths have been chosen to be closer to ones employed in [25]. Finally, the proposed pulse repetition interval (PRI), chosen to round up to the maximum range distance between target location and sensors to the successive kilometer, allows for a maximum unambiguous range of 3 km. Then, the pulse length is calculated as PRI/100.

Table 1. System Parameters.

Parameters	Values
RF Carrier (Single-band)	9 GHz
RF Carrier (Multi-band)	8, 9, 10 GHz
Modulation	Linear Frequency Chirp (LFM)
Bandwidth	600 MHz
Pulse Repetition Interval (PRI)	20 μs
Pulse Duration	200 ns
Transmitted Power	20 W
RHs antenna gain	20 dBi
System Noise	• Optical Fiber-Induced Phase Noise • Electrical Noise of RHs

The signal distribution in both abovementioned scenarios is performed by using optical fibers. The model used for calculating the optical fiber induced phase noise has been presented in [27]. Here, it has been shown that for fiber spans shorter than around 20 km, phase noise effect on coherent MIMO processing is negligible. Since our simulator is function/block oriented, in the near future, it will be possible to consider also other sources of phase noise (e.g., oscillator/circuirtry noise, wireless links among radar channels, etc.).

5. Simulation Results and Analysis

In this Section, the identified KPIs are calculated by numerical simulations implemented in MATLAB to quantify the effectiveness of the MIMO radar in the two use-case scenarios. However, before analyzing the KPIs, let us assess the performance of the updated simulation tool, since the assessment provided in Section 2.4 is based on a downscaled experimental scenario, and simulator has been significantly improved since the experiment in Section 2.4 was performed.

A further comparison is conducted between the proposed simulator and a simple study case where a 20 m tugboat was detected by the coherent MIMO radar network in the port of Livorno [26]. Results are depicted in Figure 6a,b for the real and simulated

case, respectively. In the simulator, the extended target has been simulated considering the same parameters of the real case and the same observing radar channels, which are also depicted in ground-based scenario presented in Section 4.2. The pixel size considered for the evaluation of both MIMO-AFs has been set equal to 2 m, close to the range resolution achieved with a bandwidth of 100 MHz. Unfortunately, during the tests, only the following radar channels were able to detect the target: TX3-RX3 at S and X-band and TX3-RX2 at S-band. As mentioned in the paper, RH1 was not yet operational during the tests performed in [26]; therefore, the reference point of the ENU coordinates is set at RH2, and target is considered at 375 m west and 575 m south of RH2, which can be seen from Figure 6, with red boat-like structure representing target silhouette at [−375, −575] m in ENU coordinate system.

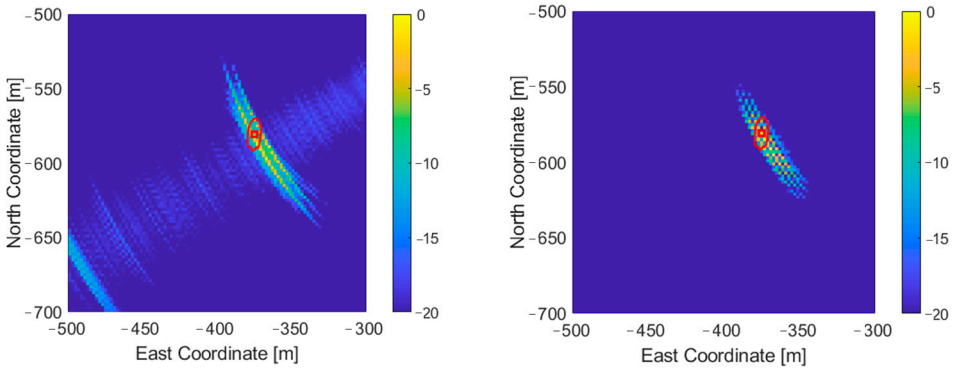

Figure 6. Dual-band MIMO Ambiguity Function for radar system deployed at Port of Livorno, Italy, and the red boat-like shape represents the target silhouettes: (**a**) Coherent MIMO processing for dual-band experimental data; (**b**) Coherent MIMO processing for dual-band simulated data.

Since RH1 is not operational and MIMO-AF is calculated only through virtual channels offered by RH2 and RH3, it results in poor aspect diversity between RH2 and RH3. The effects of this can be observed in Figure 6a, where the target is visible, but not sufficiently resolved in azimuth direction. Simulated result in Figure 6b depict a slightly better result, but again with poor azimuth resolution achieved under specific system configuration. However, the similarities between the two MIMO-AFs presented in Figure 6 highlight the effectiveness of proposed simulator in simulating close-to-reality and complex operational scenarios.

Note, that in the comparison depicted in Figure 6, an extended target model, i.e., a target occupying more than a single resolution cell was considered. However, for the sake of brevity, and for further analysis, a point-like approximation of target is considered to address the relationship between the parameters of MIMO radars and KPIs.

5.1. Single-Band MIMO Radar

Given the two MIMO radar scenarios described in Sections 4.1 and 4.2, the MIMO AFs are calculated and depicted in Figure 7a–e for the shipborne and the ground-based scenarios, respectively. The AFs for shipborne scenario are depicted for position 1 in trajectory 1 (Figure 7a) and 2 (Figure 7b), while for ground-based scenario, the AFs at position 1 (Figure 7c), 8 (Figure 7d) and 10 (Figure 7e) are shown.

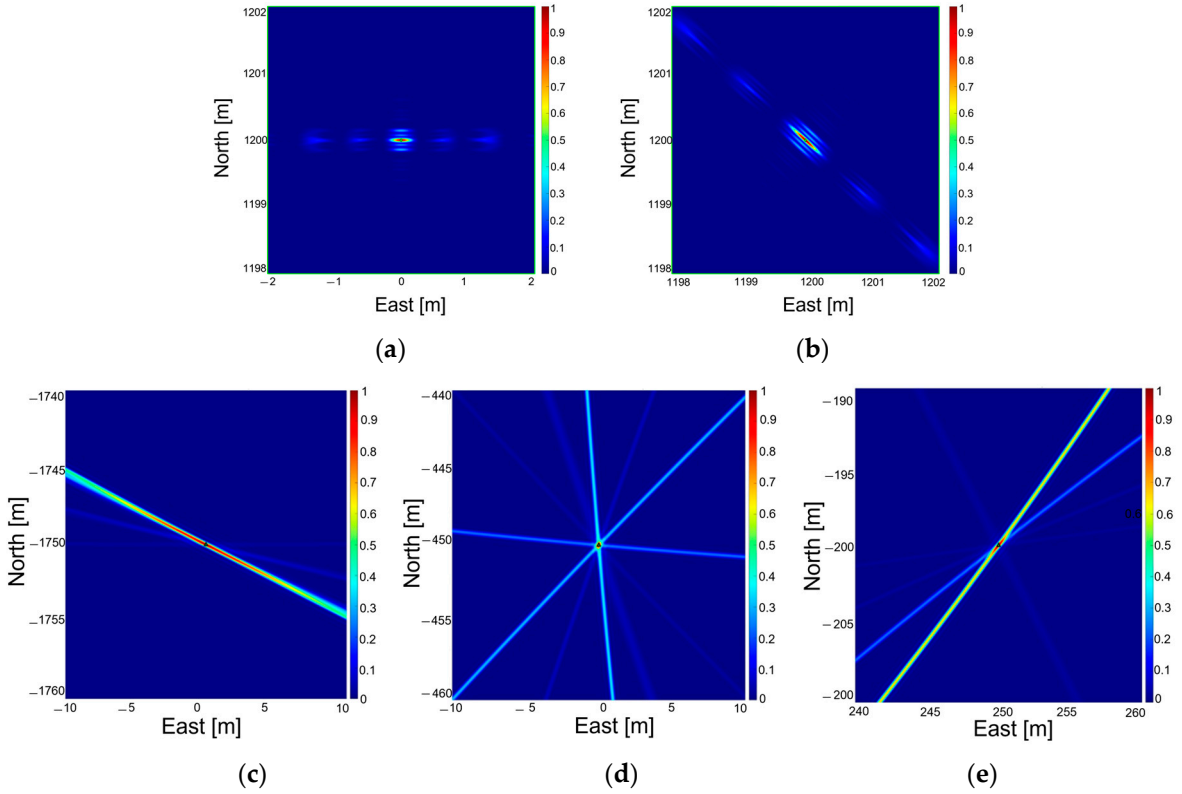

Figure 7. MIMO Ambiguity Function of coherent MIMO radar networks: (**a**) trajectory 1 with position 1 of shipborne scenario; (**b**) trajectory 2 with position 1 of shipborne scenario; (**c**) position 1 of ground-based scenario; (**d**) position 8 of ground-based scenario; and (**e**) position 10 of ground-based scenario.

Since GD describes the level of similarity among the bistatic angles subtended by all the TXs and RXs in a MIMO radar at a given target position, it is evident that the shipborne MIMO radar offers worse GD than the ground-based MIMO radar. In fact, the former can be seen as a co-located system since it employs TXs and RXs closely spaced with respect to the target distance, whereas the latter is a system with TXs and RXs widely separated with respect to the target distance. Moreover, in this latter case, when the target is moving, GD rapidly varies from point to point along the target trajectory.

The better the GD, the larger the target RCS variations at the various radar channels (i.e., TX–RX pairs); the larger the target RCS variations, the more robust the target detection capability of the MIMO radar system. However, this benefit may lead to no improvements in terms of system resolution capability with respect to the standalone radar case.

For instance, position 8 in distributed radar configuration offers better GD than that of position 1 or position 10. Although a good GD makes the system more robust against target RCS fluctuations, thus improving target-detection performance, it may severely degrade the overall resolution capability of the MIMO radar, making one (or just a few) radar channel predominant over the others, as is evident from Figure 7c–e. Instead, when GD is poor, the resolution capabilities of the system improve since the same target aspect and range are observed by all the RHs, which is evident from Figure 7a,b.

The KPIs for the shipborne MIMO radar network are depicted in Figure 8. In this case, we expect a poor GD. As a matter of fact, the varying position of the target along the trajectory with respect to RHs has little effect on the two KPIs. The PMSR and PASR are about 5 dB and 11 dB, respectively, for almost all target positions in trajectory 1. Trajectory 2 offers a slightly improved performance in terms of PASR, with PASR reaching almost 14 dB, but PMSR remains constant for both trajectories. In terms of resolution, again trajectory 1 offers slightly better performance with dXR reaching as low as 22 cm.

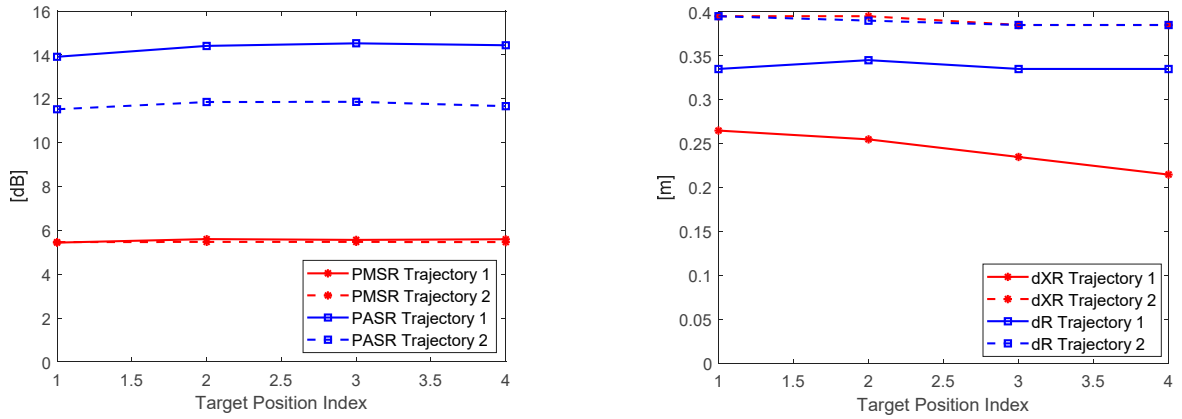

Figure 8. (**a**) PMSR (red) and PASR (blue) for co-located MIMO radar trajectory 1 (solid line) and trajectory 2 (dashed line); (**b**) d*XR* (red) and d*R* (blue) for co-located MIMO radar for trajectory 1 (solid line) and trajectory 2 (dashed line).

The KPIs for the distributed MIMO radar, i.e., ground-based scenario, are depicted in Figure 9. In this case, target position significantly affects both PMSR and PASR, as well as d*XR* and d*R*. As we could predict from Figure 9b when the target is at position 8, the system achieves better performance compared to the other target positions, thanks to a good GD. Moreover, sidelobes are significantly reduced in position 8, with PMSR and PASR of 7 dB and 9 dB, respectively (see Figure 9a). Resolutions d*XR* and d*R* are also improved with the values of 5 cm and 3 cm, respectively (see Figure 9b). However, as evident from Figure 9, for a distributed MIMO radar, performance is strongly dependent on the relative position of the target, and its orientation, with respect to the RHs.

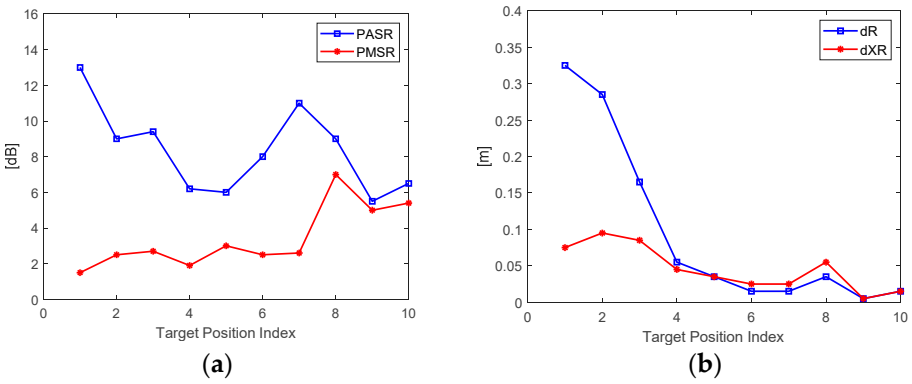

Figure 9. (**a**) PMSR (red) and PASR (blue) for distributed MIMO radar; (**b**) d*XR* (red) and d*R* (blue) for distributed MIMO radar.

5.2. Multi-Band MIMO Radar

The range and area resolutions of the target-originated peak in the case of single-band and multi-band operation are compared in Figure 10 for the ground-based MIMO radar scenario. Multi-band operation (red curves) further improves the resolution capabilities of a single-band system leveraging only on geometric diversity (blue curves).

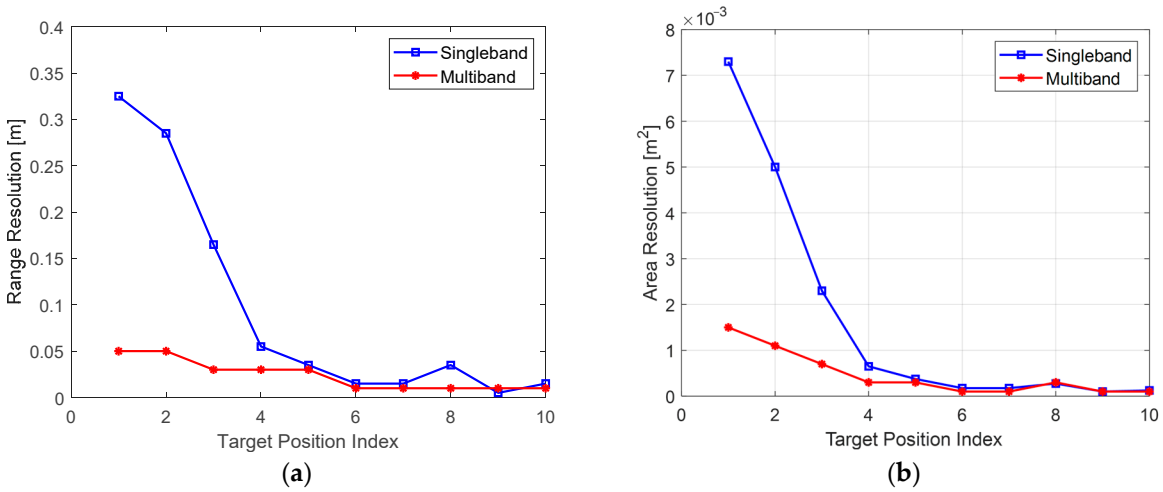

Figure 10. (**a**) dR of distributed MIMO radar at different target positions for single-band (blue) and multi-band (red) operations; (**b**) dA of distributed MIMO radar at different target positions for single-band (blue) and multi-band (red) operations.

Overall, from the results presented in Figures above, it can be concluded that co-located MIMO radars can achieve superior resolution, at the expense of detection capabilities, while distributed MIMO radars can offer robust detection capabilities but at the expense of target resolution, so a trade-off is required. However, target resolution in case of distributed MIMO radars can be improved by employing a good GD, as is the case in Figure 7d for target in position 8 of ground-based scenario, where no channel is dominant over then other.

6. Conclusions

In this work, a simulation tool in MATLAB programming language has been presented to model coherent MIMO radars based on microwave photonics techniques. In this tool, a novel approach for estimating the RCS of extended maritime targets has been proposed to reduce computational burden.

The system performance in co-located and distributed MIMO configuration, as well as in single- and multi-band operation, has been evaluated by means of relevant KPIs, which describe the characteristics of the coherent MIMO-AF.

Simulations have been carried out in two use-case scenarios: a co-located MIMO radar mounted on top of a surveillance vessel and a distributed MIMO radar deployed in a port area. The former scenario offers improved system resolution, whereas the latter offers robustness in target detection, at the cost of a potential degradation of resolution.

The proposed KPIs are analyzed in terms of both geometric and frequency diversities of the system, laying the foundations for general system optimization criteria valid in any given surveillance application.

In the future, the simulator will be further developed for considering system non-idealities and for including the multiple sources of phase noise (e.g., oscillator/circuitry noise, wireless links among radar channels, etc.).

Author Contributions: Conceptualization, M.M.H.A., S.M. and A.B.; methodology, M.M.H.A. and S.M.; software, M.M.H.A.; validation, S.M., A.M., G.P. and M.S.; formal analysis, M.M.H.A., S.M., A.M., G.P. and M.S.; investigation, M.M.H.A. and S.M.; writing—original draft preparation, M.M.H.A.; writing—review and editing, S.M., M.S. and A.B.; visualization, M.S., A.M. and A.B.; supervision, M.S. and A.B.; project administration, A.B.; funding acquisition, A.B. All authors have read and agreed to the published version of the manuscript.

Funding: This research was funded within the project COSMOS by the FISR funding scheme, Italian Ministry of University and Research, grant number FISR2019_03476.

Data Availability Statement: Not applicable.

Acknowledgments: This work was partly funded by the "EU under the Italian National Recovery and Resilience Plan (NRRP) of NextGenerationEU, partnership on "Telecommunications of the Future" (PE00000001—program "RESTART").

Conflicts of Interest: The authors declare no conflict of interest. The funders had no role in the design of the study; in the collection, analyses, or interpretation of data; in the writing of the manuscript; or in the decision to publish the results.

References

1. Skolnik, M.I. *Radar Handbook*; McGraw-Hill Education: New York, NY, USA, 2008.
2. *IEEE Std 686-2017 (Revision of IEEE Std 686-2008)*; IEEE Standard for Radar Definitions. IEEE: New York, NY, USA, 13 September 2017; pp. 1–54. [CrossRef]
3. Li, J.; Stoica, P. MIMO Radar with Colocated Antennas. *IEEE Signal Process. Mag.* **2007**, *24*, 106–114. [CrossRef]
4. Haimovich, A.M.; Blum, R.S.; Cimini, L.J. MIMO Radar with Widely Separated Antennas. *IEEE Signal Process. Mag.* **2008**, *25*, 116–129. [CrossRef]
5. He, Q.; Yang, Y.; Blum, R.S. MIMO Radar with Widely Separated Antennas—From Concepts to Designs. In *Book Chapter for E-Reference Signal Processing*; Elsevier Science Direct: Amsterdam, The Netherlands, 2014.
6. Capmany, J.; Novak, D. Microwave photonics combines two worlds. *Nat. Photonics* **2007**, *1*, 6. [CrossRef]
7. Zhang, F.; Gao, B.; Pan, S. Photonics-based MIMO radar with high-resolution and fast detection capability. *Opt. Express* **2018**, *26*, 17529–17540. [CrossRef] [PubMed]
8. Nie, H.; Zhang, F.; Yang, Y.; Pan, S. Photonics-based integrated communication and radar system. In Proceedings of the 2019 International Topical Meeting on Microwave Photonics (MWP), Ottawa, ON, Canada, 7–9 October 2019; pp. 1–4. [CrossRef]
9. Serafino, G.; Maresca, S.; Amir, M.M.H.; Malacarne, A.; Ghelfi, P.; Bogoni, A. Key Performance Indicators for System Analysis of MIMO Radars with Widely Separated Antennas. In Proceedings of the 2022 19th European Radar Conference (EuRAD), Milan, Italy, 28–30 September 2022; pp. 1–4. [CrossRef]
10. Berry, P.E.; Dahal, N.; Venkataraman, K. On the design of an optimal coherent multistatic radar network configuration. *IET Radar Sonar Navig.* **2022**, *16*, 869–884. [CrossRef]
11. Sharma, V.; Kbashi, H.J.; Sergeyev, S. MIMO-employed coherent photonic-radar (MIMO-Co-PHRAD) for detection and ranging. *Wirel. Netw.* **2021**, *27*, 2549–2558. [CrossRef]
12. Simulate an Automotive 4D Imaging MIMO Radar—MATLAB & Simulink—MathWorks Italia. Available online: https://it.mathworks.com/help/radar/ug/simulate-an-automotive-4d-imaging-mimo-radar.html#SimulateAnAutomotive4DImagingMIMORadarExample-11 (accessed on 4 August 2023).
13. Chen, H.; Zhao, Y.; Li, D.; Liu, C.; Wang, W. Least squares approach to the design of frequency invariant beamformer with sensor delay lines in subbands. In Proceedings of the IET International Radar Conference 2013, Xi'an, China, 14–16 April 2013; pp. 1–8. [CrossRef]
14. Kılıç, B.; Arıkan, O. Capon's Beamformer and Minimum Mean Square Error Beamforming Techniques in Direction of Arrival Estimation. In Proceedings of the 2021 29th Signal Processing and Communications Applications Conference (SIU), Istanbul, Turkey, 9–11 June 2021; pp. 1–4. [CrossRef]
15. Zhang, J.; Hao, Y.; Sun, S.; Liu, X. Self-steered Robust Capon Beamformer against Large Look Direction Error. In Proceedings of the 2023 4th Information Communication Technologies Conference (ICTC), Nanjing, China, 17–19 May 2023; pp. 228–231. [CrossRef]
16. Knott, E.F. *Radar Cross Section*, 2nd ed.; Artech House: Boston, MA, USA, 1993.
17. Mahafza, B.R. *Radar Systems Analysis and Design Using MATLAB*, 3rd ed.; Chapman and Hall/CRC: New York, NY, USA, 2013.
18. Ahmed, T.I.O.; Mirghani, M. Estimation of Radar Cross Sectional Area of Target using Simulation Algorithm. *Int. J. Res. Stud. Electr. Electron. Eng.* **2018**, *4*, 20–24.
19. Jenn, D. POfacets4.5. MATLAB Central File Exchange. 2023. Available online: https://www.mathworks.com/matlabcentral/fileexchange/50602-pofacets4-5 (accessed on 4 August 2023).
20. Nathanson, F.E.; Reilly, J.P.; Cohen, M.N. *Radar Design Principles: Signal Processing and the Environment*, 2nd ed.; McGraw-Hill, Inc.: New York, NY, USA, 1991.
21. Williams, P.D.L.; Cramp, H.D.; Curtis, K. Experimental study of the radar cross-section of maritime targets. *IEE J. Electron. Circuits Syst.* **1978**, *2*, 121. [CrossRef]
22. Chatzigeorgiadis, F. Development of Code for a Physical Optics Radar Cross Section Prediction and Analysis Application. Master's Thesis, Naval Postgraduate School, Monterey, CA, USA, 2004.
23. Ewell, G.; Zehner, S. Bistatic radar cross section of ship targets. *IEEE J. Ocean. Eng.* **1980**, *5*, 211–215. [CrossRef]
24. Willis, N.J. *Bistatic Radar*; SciTech Publishing: Raleigh, NC, USA, 2005.
25. Malacarne, A.; Maresca, S.; Scotti, F.; Ghelfi, P.; Serafino, G.; Bogoni, A. Coherent Dual-Band Radar-Over-Fiber Network With VCSEL-Based Signal Distribution. *J. Light. Technol.* **2020**, *38*, 6257–6264. [CrossRef]

26. Maresca, S.; Serafino, G.; Noviello, C.; Scotti, F.; Fornaro, G.; Sansosti, E.; Bogoni, A.; Ghelfi, P. Field Trial of a Coherent, Widely Distributed, Dual-Band Photonics-Based MIMO Radar with ISAR Imaging Capabilities. *J. Light. Technol.* **2022**, *40*, 6626–6635. [CrossRef]
27. Malacarne, A.; Maresca, S.; Pandey, G.; Amir, M.M.H.; Bogoni, A.; Scaffardi, M. Robustness of Photonics-based Coherent Multi-Band MIMO Radar to Fiber-based Signal Distribution. In Proceedings of the European Radar Conference (EuRAD), Berlin, Germany, 20–22 September 2023.